

# Magnetic reconnection during collisionless, stressed, X-point collapse using Particle-in-Cell simulation

D. Tsiklauri and T. Haruki

*Institute for Materials Research, University of Salford, Manchester, M5 4WT, Great Britain*

(Dated: April 26, 2019)

Magnetic reconnection during collisionless, stressed, X-point collapse was studied using kinetic, 2.5D, fully electromagnetic, relativistic Particle-in-Cell numerical code. Two cases of weakly and strongly stressed X-point collapse were considered. Here descriptors weakly and strongly refer to 20 % and 124 % unidirectional spatial compression of the X-point, respectively. In the weakly stressed case, the reconnection rate, defined as the out-of-plane electric field in the X-point (the magnetic null) normalised by the product of external magnetic field and Alfvén speeds, peaks at 0.11, with its average over 1.25 Alfvén times being 0.04. During the peak of the reconnection, electron inflow into the current sheet is mostly concentrated along the separatrices until they deflect from the current sheet on the scale of electron skin depth, with the electron outflow speeds being of the order of the external Alfvén speed. Ion inflow starts to deflect from the current sheet on the ion skin depth scale with the outflow speeds about four times smaller than that of electrons. Electron energy distribution in the current sheet, at the high-energy end of the spectrum, shows a power law distribution with the index varying in time, attaining a maximal value of  $-4.1$  at the final simulation time step (1.25 Alfvén times). In the strongly stressed case, magnetic reconnection peak occurs 3.4 times faster and is more efficient. The peak reconnection rate now attains value 2.5, with the average reconnection rate over 1.25 Alfvén times being 0.5. Plasma inflow into the current sheet is perpendicular to it, with the electron outflow seeds reaching 1.4 Alfvén external Mach number and ions again being about four times slower than electrons. The power law energy spectrum for the electrons in the current sheet attains now a steeper index of  $-5.5$ , a value close to the ones observed near X-type region in the Earth's magneto-tail. Within about one Alfvén time, 2% and 20% of the initial magnetic energy is converted into heat and accelerated particle energy in the case of weak and strong stress, respectively. In the both cases, during the peak of the reconnection, the quadruple out-of-plane magnetic field is generated, hinting possibly to the Hall regime of the reconnection. These results strongly suggest the importance of the collisionless, stressed X-point collapse as an efficient mechanism of converting magnetic energy into heat and super-thermal particle energy.

PACS numbers: 52.35.Vd; 96.60.Iv; 52.65.Rr; 45.50.Dd; 96.60.pf; 96.60.qe

## I. MOTIVATION OF THE STUDY

Magnetic reconnection is an important physical process, which serves as one of the possible ways of converting energy stored in the magnetic field into heat and non-thermal, accelerated, motion of plasma particles. This process operates virtually in all extra-galactic, stellar, solar, space and laboratory plasmas with varied degree of importance. For example, in solar and stellar flares magnetic reconnection plays a key role. In addition, it can be one of the main contributing factors to solar coronal heating problem amongst other mechanisms such as wave dissipation. As far as plasma heating is concerned, in the collisional regime, be it Tokamak plasma or solar corona (which perhaps is better described as a collisionless medium), Spitzer resistivity is  $\propto T_e^{-3/2}$ , where  $T_e$  is the electron temperature. Thus, in becoming hotter, plasma essentially starts to behave as a superconductor, i.e. further heating (increase in temperature) is impeded due to decrease of the resistive properties. In this context, a direct conversion of magnetic energy into heat via reconnection seems rather attractive. As far as the particle acceleration is concerned, 50-80 % of the energy released during solar flares is converted into the energy of accelerated particles. Thus, knowledge of the details of

particle acceleration via magnetic reconnection (which is deemed as a major mechanism operating solar and stellar flares) is also important.

The main aspects of the reconnection process can be classified as whether it is resistive (collisional) or collisionless; spontaneous or forced; and/or steady or time-dependent. Each of these aspects have been studied extensively with varied level of progress. For example, both steady and time-dependent, *resistive* reconnection processes are very well studied [see e.g. Ref.[1] and references therein], while it is only recently some progress has been made in the study of *collisionless* reconnection [see e.g. Ref.[2, 3] and references therein]. This can be explained by the fact that resistive reconnection is simpler in its nature. Changing structure (connectivity) of magnetic field lines, which essentially is the reconnection, requires some mechanism (dissipation) to break the frozen-in condition. In the case of resistive reconnection it is  $\eta \vec{j}$  term. In fact, rate at which reconnection proceeds is given by an inflow velocity into the dissipation region  $v_{in} \simeq (\delta/\Delta)v_A$ , where  $\delta$  and  $\Delta$  are width and length of the region, and  $v_A$  is Alfvén speed. In the simplest resistive, steady model of Sweet-Parker  $\delta \simeq \eta^{1/2}$  and  $\Delta \simeq L$ , where  $L$  is the macroscopic system size. In the collisionless regime however, other terms in the Ohm's law, such as electron inertia

term, Hall term and electron pressure tensor become far more important than the usual  $\eta \vec{j}$  term on which resistive reconnection models rely. Each of these terms has an associated spatial scale with them, i.e. scale at which they start to play a dominant role. For example, electron inertia term is associated with the electron skin depth  $c/\omega_{pe}$ , Hall term is with the ion skin depth  $c/\omega_{pi}$ , while electron pressure tensor is with ion Larmor radius [see e.g. p. 87 in Ref.[3] or p. 42 in Ref.[1]].

One of the main outcomes of recent research in collisionless reconnection can be summarised by GEM [4, 5] and Newton [6] reconnection challenges. These considered the same physical system: Harris-type equilibrium with anti-parallel magnetic field, relevant to geomagnetic tail application, with finite initial magnetic perturbations in the case of GEM challenge and time-transient inhomogeneous, driven inflow of magnetic flux in the case of Newton challenge. The novelty of the approach was to use different numerical codes [MHD, Hall MHD, Hybrid and Particle-in-Cell (PIC)], in order to pin-point essential physical mechanism that facilitates the reconnection. These works established that as long as dispersive whistler waves are included (these can only appear if one allows for the different dynamics for electrons and ions), the rate at which reconnection proceeds does not change, irrespective of which term breaks the frozen-in condition.

Yet another interesting analytical result corroborated by the numerical simulations is that in 2D steady reconnection, Petschek reconnection rate functional form remains the same when the Hall term is included (in the Hall MHD model), but what changes is the length from the X-point to the start of slow mode shocks [7]. In MHD, this length is the half width of the resistive region,  $L_R$ , but when Hall term is included the length is replaced by  $L_R + c/\omega_{pi}$  [7]. This important result essentially provides an analytical scaling for the collisionless reconnection (when  $\eta$  is zero) for such physical system. Thus, future kinetic studies that use PIC simulation need to corroborate it. Ref.[7] already tested this scaling law via MHD and Hall MHD simulation.

Importance of the electron inertia in the X-point with finite out-of-plane guide magnetic field has been investigated in Ref.[8]. Particularly noteworthy result was that when the normalised collisionless electron skin depth  $[c/(\omega_{pe}L)]$  exceeds the dimensionless resistive length scale ( $S^{-1/2}$ ), where  $S$  is the Lindquist number, the energy in a shear Alfvén wave approaching an X-point is rapidly transformed into plasma kinetic energy and heat. Assuming solar coronal parameters, the normalised electron skin depth is  $10^{-8}$  (assuming  $L = 10$  Mm and  $c/\omega_{pe} = 0.1$  m), while dimensionless resistive length scale is  $3 \times 10^{-7}$  (in the corona typically  $S = 10^{13}$ ). Thus, the proposed in [8] may well be effective.

Previous works on particle acceleration mostly focused on test-particle type calculations of the particle trajectories in different 2D [9, 10, 11, 12] or more recently 3D [13, 14, 15, 16] magnetic reconnection configurations. In such approach feedback on reconnection electromag-

netic (EM) fields from motion (spatial redistribution) of charged particles is ignored. Our approach does not suffer from this drawback, as we use fully electromagnetic, relativistic PIC numerical code in which EM fields are calculated at each step from the spatial distribution of the charges.

According to Ref.[1], resistive time-dependent reconnection other than well known tearing mode can be split into two main classes: X-type collapse, which was first considered by Ref.[17] (a decade before tearing mode was discovered) and Petschek-type theory developed by Ref.[18]. Previous work on X-point collapse is well described in chapter 7.1 of Ref.[1]. Also see more recent work on the subject [19]. A good example of combination of analytical and numerical work on magnetic reconnection at stressed X-type neutral points can be found in Ref.[20]. Boundary conditions used in Ref.[20], where such that they did not allow for flux or mass flow through the boundary. The studies with closed boundaries are physically justified by being isolated systems, whereas some of those with open boundaries lead to misleading results: for example, in an open system a potential X-point can collapse due to inflow of energy from outside.

Initial analytical work on this topic considered unbounded self-similar solutions. These indicated that  $E_z(0, 0, t)$ , the out-of-plane electric field at the magnetic null, which is the measure of reconnection rate, tends to infinity as  $t \rightarrow \infty$  [e.g. Fig.(7.3) from Ref.[1]]. The main outcomes of the previous, stressed X-point collapse in the resistive MHD (in the case of low-resistivity and low-beta) can be summarised as following:

(i) The X-point collapse is different depending whether initial stressing is weak or strong. In the weak case the average reconnection rate scale as  $1/\ln(\bar{\eta})$ , where  $\bar{\eta} = 1/S$  is the dimensionless resistivity [ $\bar{\eta} = \eta/(V_{A0}L) = 1/S$ ], while strong case it is independent of  $\bar{\eta}$ .

(ii) There is an issue related to efficiency of the process: Ref.[21] showed that for fast reconnection to occur  $\beta < \bar{\eta}^{0.565}$ , otherwise pressure in the current sheet chokes off the collapse process. For solar coronal conditions,  $\bar{\eta} \simeq 10^{-13}$  this requires  $\beta < 10^{-8}$ , which is too low to match the observed values circa 0.01 – 0.001. However, this shortcoming seems to be alleviated by inclusion of non-linear effects, i.e. case of strong perturbations (strong stressing) [21]. If the compression is sufficiently large, magnetic pressure of the imploding wave expels trapped gas in the current sheet from its ends, allowing it to thin and faster reconnection to occur.

Motivation of the present study is five-fold:

(i) Naturally, different boundary and initial conditions produce different scaling of reconnection rate e.g. with resistivity (in the case of resistive reconnection). To our knowledge X-type collapse by a uniform stress (compression) along one of the axis, as described in chapter 2.1 in Ref.[1], has not been investigated numerically neither in the case of resistive (MHD) reconnection, nor in the collisionless regime;

(ii) This type of stress (compression) is likely to occur

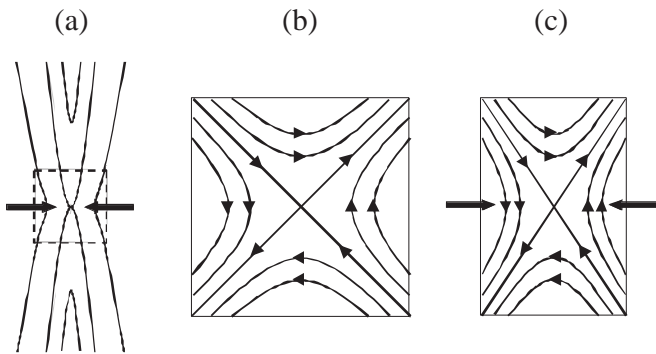


FIG. 1: Magnetic field line geometry. (a) A portion of a standard Solar flare model with added compressions on sides. The bottom part mimics the footpoints of a coronal loop, with an X-point on top (inside the dashed box). Two arrows indicate compression direction. A dashed box is the region which our study tries to mimic by uniform stress in one direction [see (c)]. (b) Magnetic field configuration for stress parameter  $\alpha = 1$ , which is stable (no X-point collapse occurs). (c) Magnetic field configuration for stress parameter  $\alpha > 1$ . Such X-point collapses under high magnetic pressure/tension forces.

in the framework of a flare model (see details below).

(iii) To our knowledge the most of previous collisionless reconnection studies considered anti-parallel, Harris type magnetic field configuration, which is more relevant to Earth magneto-tail application. For solar and stellar flares X-type configuration is more relevant.

(iv) Some of the models of coronal mass ejections [22] which use motion of photospheric footpoints as a driver, end up with situation physically similar to stressed X-point collapse (strictly speaking Y-points occur there).

(v) We aimed to investigate properties of the accelerated particles in the current using self-consistent electromagnetic fields, as a further extension of the test-particle type approach.

## II. SIMULATION MODEL

### A. Stressed X-point reconnection model

Fig. 1 represents magnetic field line geometry considered in this paper. In order to study stressed magnetic reconnection, we consider a magnetic X-point collapse which may naturally occur during solar flares [see sketch in Fig. 1(a)]. Such stressed X-point may occur e.g. if photospheric footpoints of the coronal loops move towards each other (e.g. pushed by convective motions) or some compression from the sides in the corona forces them to do so. We study dynamics of such stressed X-point by means of kinetic, 2.5D, fully electromagnetic, relativistic Particle-in-Cell numerical code. We focus attention on the local region inside the dashed box which is the region that our study tries to mimic by uniform stress in one direction [see Fig. 1(c)]. If there is no stress from

the sides the considered magnetic configuration is stable [Fig. 1(b)]. Interestingly, Ref.[23] investigated what happens when a fast magnetosonic shock wave associated with a coronal mass ejection collides obliquely with a coronal streamer with a stable current sheet. Their set up is somewhat analogous to ours, but much more violent, as we only consider X-point compression, while they blasted it with a Alfvén Mach 6 shock.

The initial magnetic field configurations used are

$$B_x = \frac{B_0}{L}y, \quad B_y = \frac{B_0}{L}\alpha^2x, \quad B_z = 0, \quad (1)$$

where  $B_0$  is magnetic field intensity at the distance  $L$  from the X-point for  $\alpha = 1.0$ ,  $L$  is the global external length-scale of reconnection, and  $\alpha$  is the stress parameter [see chapter 2.1 in Ref.[1]]. In addition, the uniform current is imposed at  $t = 0$  in the  $z$ -direction,

$$j_z = \frac{B_0}{\mu_0 L}(\alpha^2 - 1). \quad (2)$$

This current appears because of the stress imposed on magnetic field lines.

### B. PIC simulation code

The simulation code used here is 2.5D relativistic and fully electromagnetic PIC code, modified from the 3D TRISTAN code [24]. In this code, both the electron and ion dynamics are described as particles. Equation of motion for each particle is solved using self consistent electromagnetic fields,

$$\frac{d\vec{v}_{si}}{dt} = \frac{q_s}{m_s}(\vec{E} + \vec{v}_{si} \times \vec{B}), \quad (3)$$

$$\frac{d\vec{r}_{si}}{dt} = \vec{v}_{si}, \quad (4)$$

$$\frac{\partial \vec{E}}{\partial t} = c^2 \nabla \times \vec{B} - \frac{1}{\epsilon_0} \sum_s \vec{j}_s, \quad (5)$$

$$\frac{\partial \vec{B}}{\partial t} = -\nabla \times \vec{E}, \quad (6)$$

where  $\vec{E}$ ,  $\vec{B}$ ,  $\vec{j}_s$ ,  $\vec{v}_{si}$  and  $\vec{r}_{si}$  are electric and magnetic fields, current density, particle velocity and position, respectively. The subscript  $s$  represents species of plasma, that is  $s = e$  for electron and  $s = i$  for ion. The subscript  $i$  indicates  $i$ -th particle index. The other quantities,  $q_s$ ,  $m_s$ ,  $c$ ,  $\epsilon_0$ , are charge and mass of a plasma particle, speed of light, vacuum permittivity, respectively. In addition to above Eqs. (3)–(6),  $\nabla \cdot \vec{B} = 0$  and  $\nabla \cdot \vec{E} = \rho_e/\epsilon_0$  must be satisfied initially ( $\rho_e$  is charge density, which is taken as 0). The latter two conditions are automatically

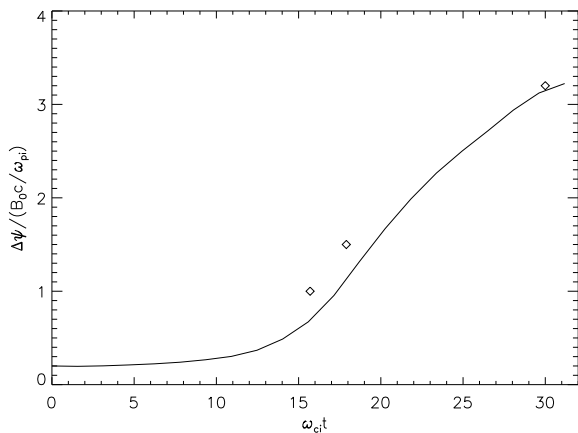


FIG. 2: Time evolution of the reconnected magnetic flux difference. The horizontal axis is time normalised by the ion cyclotron frequency,  $\omega_{ci}$ . The solid curve is the magnetic flux difference,  $\Delta\psi$ , between the O and X lines, which is normalised by  $B_0c/\omega_{pi}$ , using our PIC code. Open squares correspond to published GEM challenge values.

satisfied at all times due to the nature of the numerical scheme used [24]. Electromagnetic fields which satisfy Eqs. (5)–(6) update particle velocity through the equation of motion Eq. (3), which in turn updates particle positions Eq. (4). Repeating this procedure many times mimics plasma particle dynamics in self-consistent electromagnetic fields.

We started by testing our code, reproducing published GEM challenge results [4, 5]. Fig. 2 shows time evolution of the reconnected magnetic flux difference between and O and X-lines. Open squares correspond to the published GEM challenge values. We gather from this graph that match between our simulation results and that of GEM challenge [4, 5] is good. We could also reproduce other figures from Refs.[4, 5], thus we were reasonably confident to start a new X-point collapse simulation, which is the subject of the present paper.

The length of the system in two dimensions is  $L_x = L_y = 400\Delta$  (this is excluding, so called, ghost cells needed for updating the boundary conditions), where  $\Delta = 1$  is the simulation grid size corresponding to electron Debye length,  $\lambda_D = v_{te}/\omega_{pe} = 1\Delta$  ( $v_{te}$  is electron thermal velocity and  $\omega_{pe}$  is electron plasma frequency). The global external length-scale of reconnection is set  $L = 200\Delta$ . Number density is fixed at  $n_0 = 100$  electron-ion pairs per cell. Both electrons and ions are uniformly distributed throughout the system, hence total number is 1.6 million pairs.

Zero-gradient boundary conditions are imposed both on the electric and magnetic fields in  $x$ - and  $y$ -directions. Also, tangential component of electric field was forced to zero, while normal component of magnetic field was kept constant, both at the boundary. This ensures that there is no magnetic flux

through the simulation boundary, i.e. the system is isolated and  $-\int_{-L}^L B_y(x', -L, t)dx' - \int_{-L}^L B_y(x', L, t)dx' + \int_{-L}^L B_x(-L, y', t)dy' + \int_{-L}^L B_x(L, y', t)dy' = 0$ , at every time step. The latter sum is the magnetic flux on the boundary. Reflecting boundary conditions are imposed on particles in both the  $x$ - and  $y$ -directions. The latter ensures there is no mass flow across the boundary.

The simulation time step is  $\omega_{pe}\Delta t = 0.05$ . Ion to electron mass ratio is  $m_i/m_e = 100$ . Electron thermal velocity to speed of light ratio is  $v_{te}/c = 0.1$ . Electron and ion skin depths are  $c/\omega_{pe} = 10\Delta$  and  $c/\omega_{pi} = 100\Delta$ , respectively. Electron cyclotron frequency to plasma frequency ratio is  $\omega_{ce}/\omega_{pe} = 1.0$  for magnetic field intensity,  $B = B_0$ . The latter ratio is indeed close to unity in the solar corona, while it is much bigger than unity in the Earth magnetosphere. Electron and ion Larmor radii are  $v_{te}/\omega_{ce} = 1\Delta$  and  $v_{ti}/\omega_{ci} = 10\Delta$ , where  $v_{ti}$  is the ion thermal velocity. The temperatures of ions and electrons are the same,  $T_e = T_i$ . At the boundary the plasma  $\beta = 0.02$  and Alfvén velocity,  $V_{A0}/c = 0.1$ . Naturally these vary across the simulation box as the background magnetic field is a function of  $x$  and  $y$ .

In what follows, for the visualisation purposes, all spatial coordinates will be normalised by electron skin depth  $c/\omega_{pe}$ , while time is normalised by the inverse of plasma electron frequency  $\omega_{pe}^{-1}$ .

### III. SIMULATION RESULTS

We investigated three X-point collapse cases with different stress parameters,  $\alpha = 1.00$  (stable), 1.20 (weakly stressed) and 2.24 (strongly stressed). For  $\alpha = 1.00$ , we confirmed that the system is stable at least for  $t \leq 500$ , and no magnetic reconnection takes place. Ref.[21] has shown that when perturbations (exerted stress on an X-point) are small  $\varepsilon \sim (1 - \alpha^2) < \bar{\eta}$  then the (average) reconnection rate scales as  $1/\ln(\bar{\eta})$ , while if they are large  $\varepsilon = (1 - \alpha^2) > \bar{\eta}$  then the reconnection rate is independent of  $\bar{\eta}$ . This difference in behaviour points to a different relative importance of the physical mechanisms in action. The two different (weakly and strongly compressed) cases studied in this paper attempt the same approach as in Ref.[21]. However, one should realise that we use vastly different physical description. Ref.[21] uses resistive MHD, while our PIC (fully kinetic) approach is collisionless, and, in turn, in our case  $\bar{\eta} = 0$ . However, it has been observed before, that often scattering of plasma particles from the magnetic field lines, plays effective role of collisions. E.g. Refs.[25, 26] have shown that the Alfvén wave dissipation in the collisionless case (using the same PIC, kinetic code) follows scaling law which is the same as in resistive MHD case [27]. At the same time, this is not to say that we are confident that the effective particle scattering off the magnetic fields, which mimics resistive (collisional) effects, is the mechanism that breaks down the frozen-in condition here. The

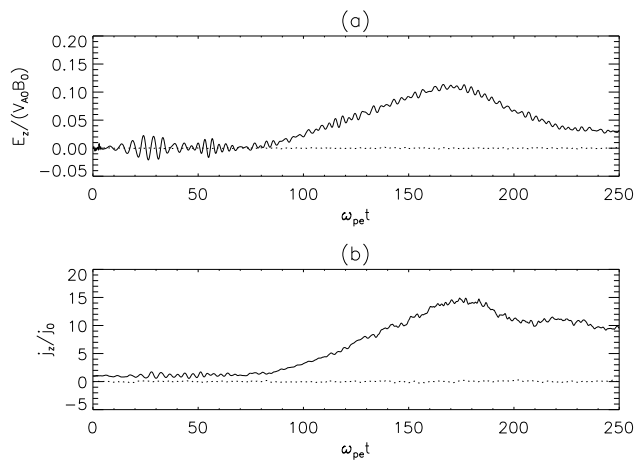


FIG. 3: (a) Time evolution of the reconnection rate, defined as the out-of-plane electric field in the X-point,  $E_z(0, 0, t)$  normalised by the product of external magnetic field and Alfvén speeds (both at the boundary for  $\alpha = 1.00$ ) for  $\alpha = 1.20$  (solid line) and  $\alpha = 1.00$  (dotted line). (b) Time evolution of total current density,  $j_z$ , in the X-point for  $\alpha = 1.20$ . Note that final simulation time  $t = 250$  corresponds to  $t/\tau_A = 1.25$ , with the latter being the Alfvén time.

issue of which term in the generalised Ohm’s law is responsible for the reconnection in the collisionless stressed X-point collapse will be studied separately.

### A. Weakly stressed X-point case ( $\alpha = 1.20$ )

It should be noted that  $\alpha$ , the measure of stress, is essentially the aspect ratio of the compression, i.e. since the limiting magnetic field lines are given by  $y = \alpha x$ ,  $\alpha = 1.2$  means  $1.2-1.0=0.2$  i.e. 20% compression of the X-point in  $x$ -direction. Similarly,  $\alpha = 2.24$  case represents 124% compression, i.e. 1.24 times stressed.

Also, because change in  $\alpha$  means change of strength of the magnetic field on the boundary, the external Alfvén speed also changes. E.g. we fixed Alfvén velocity,  $V_{A0}/c = 0.1$  for  $\alpha = 1$ , but for  $\alpha > 1$ ,  $V_{A0}/c = \sqrt{(1 + \alpha^4)/2} \times 0.1$ . This for  $\alpha = 1.20$ ,  $V_{A0}/c = 0.124$ , but for  $\alpha = 2.24$ ,  $V_{A0}/c = 0.36$ .

Fig. 3(a) shows time evolution of the reconnection rate, defined as the out-of-plane electric field in the X-point,  $E_z(0, 0, t)$  normalised by the product of external magnetic field and Alfvén speeds (both at the boundary), i.e. by  $E_0 = V_{A0}B_0$ , for  $\alpha = 1.20$  (solid line) and  $\alpha = 1.00$  (dotted line). Because usually PIC simulation suffers for large (thermal) noise especially towards high energy ends of the particle distribution function, a boxcar average scheme with width 150 mesh points was applied for smoothing the line-data. Mind that this does not alter absolute value of the peak at  $t = 170$ . Our normalisation of the electric field is such that effectively Fig. 3(a) shows the Alfvén Mach number of the inflowing plasma,

$M_A$ , i.e.  $E/E_0 = v/V_{A0} = M_A$ . This follows from a typical estimate  $E \simeq vB_0 \simeq M_A V_{A0} B_0$  [e.g. Ref.[10]]. We gather from this figure that for the case of  $\alpha = 1$  no  $E_z$  is generated, as such configuration is stable and no X-point collapse or reconnection occurs (dotted line). On contrary, for the case of  $\alpha = 1.2$  we see that the reconnection rate peaks at about 0.11 at  $t = 170$  which is the same as  $t/\tau_A = 0.85$ . Here  $\tau_A$  is the Alfvén time – the distance from the outer boundary to the X-point (20) divided by the Alfvén speed at the boundary ( $V_{A0} = 0.1c$ ). We also calculated the average reconnection rate based on Fig. 3(a). It is defined as

$$E_{av} = \frac{1}{t_f} \int_0^{t_f} \frac{E_z(0, 0, t)}{E_0} dt, \quad (7)$$

where  $t_f = 250$  is the final simulation time. This yields  $E_{av} = 0.04$ , a relatively small value.

Fig. 3(b) shows time evolution of total current density,  $j_z$ , in the X-point for  $\alpha = 1.20$  (solid line) and  $\alpha = 1.0$  (dotted line). The total current density is normalised by the initial value,  $j_0 = n_0 e v_{d0}$ ,  $v_{d0}$  is the drift velocity. As expected  $\alpha = 1$  case stays current free throughout the simulation, while  $\alpha = 1.2$  produces a peak current of  $j_z/j_0 = 15$  and then subsequently decays off.

It should be noted that we have performed one additional numerical run with  $\alpha = 1.2$ , but without imposing initial  $j_0$  current prescribed by Eq.(2). This is because e.g. one might expect that in a X-point above the arcade of loops in the solar corona, only compression (stress) of the magnetic field from the two sides is likely. Such perturbation violates the equations at  $t = 0$ , this results in a large spike of magnitude 0.22 at  $t = 5$  in the equivalent version of Fig. 3(a) (not presented here). Otherwise, for  $t > 5$  there was no noticeable difference between the cases with and without imposing the initial current. Thus, in what follows we only discuss cases with the current imposed at  $t = 0$ .

Fig. 4 shows time evolution of spatial distribution of total current density,  $j_z$ , in the  $x$ - $y$  plane at (a)  $t = 0$ , (b) 100, (c) 170 and (d) 250 for  $\alpha = 1.20$ . The current flows uniformly in the  $z$ -direction Fig. 4(a), with drift velocity is  $v_{d0}/c = 0.022$ . We assumed that half of the drift velocity comes from electrons and another half from ions, i.e.  $v_{de0} = 0.5v_{d0}$  and  $v_{di0} = 0.5v_{d0}$ . Fig. 4(b) shows that the current begins to focus in the X-point because of high magnetic pressure/tension. The current peaks in the current sheet attaining  $j_z/j_0 = 15$  at  $t = 170$ , as seen in Fig. 4(c). In the later phases, the current sheet tends to decay [Fig. 4(d)]. This figure is useful for visualising the spatial dimensions of the current sheet. In turn, this enables to make the following useful estimate: From Fig. 4(c) (peak current time snapshot) we gather that the width of the current sheet (in horizontal direction) is about electron skin-depth  $\delta \simeq 1.4$ , while its length (in vertical direction) is about  $\Delta \simeq 10$ . To be precise, we actually measured  $\delta$  and  $\Delta$  by more accurate means: we looked at line plots of  $j_z(x, 0)$  and  $j_z(0, y)$  respectively, at  $t = 170$ , and measured appropriate half-width of the

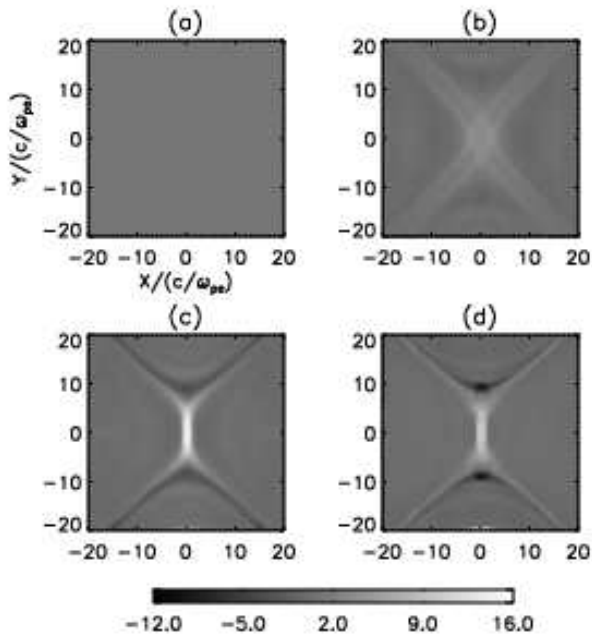


FIG. 4: Time evolution of the spatial distribution of total current density,  $j_z$ , in the  $X$ - $Y$  plane at (a)  $t = 0$ , (b) 100, (c) 170 and (d) 250 for  $\alpha = 1.20$ . The total current density is normalised by the initial value,  $j_0 = n_0 e v_{A0}$ .

$j_z(x, 0)$  and  $j_z(0, y)$  peak (in both  $x$  and  $y$ -directions). The ratio of the two gives the inflow Alfvén Mach number  $M_A \simeq \delta/\Delta \simeq 0.14$ . This is very close to the peak value of  $E/E_0 = v/V_{A0} = M_A = 0.11$  [from Fig. 3(a)]. We thus measured the peak reconnection rate by two *independent* means directly from the simulation [using Fig. 3(a)] and using the steady reconnection formula  $M_A \simeq \delta/\Delta$  [e.g. Eq.(3.1) from Ref.[3]]. The close match points to the fact that nearly steady reconnection regime is achieved in the vicinity of the peak at  $t = 170$ .

Fig. 5 shows the time evolution of spatial distribution of the out-of-plane magnetic field,  $B_z$ , at (a)  $t = 0$ , (b) 100, (c) 170 and (d) 250 for  $\alpha = 1.20$ . Time of each panel in Fig. 5 corresponds to those of Fig. 4, respectively. As can be seen in Fig. 5(a) initially there is no out-of-plane magnetic field present. Then, Fig. 5(b) shows that the quadruple magnetic field structure appears, which is the most pronounced at  $t = 170$  [Fig. 5(c)]. This structure is a well known signature of a magnetic reconnection in the Hall MHD regime. Ref.[28] showed that as long as one allows for different electron and ion dynamics (two-fluid description) i.e. when Hall term is non-zero such quadruple out-of-plane magnetic field is generated.  $B_z$  attains a value of  $|B_z|/B_0 = 0.18$  at  $t = 170$  and then subsequently decays, Fig. 5(d), (as well as the current sheet).

In Fig. 6 we show dynamics of individual magnetic field lines. We tried to trace dynamics of several magnetic field lines in order to visualise the reconnection process. We can clearly see that magnetic field lines come towards

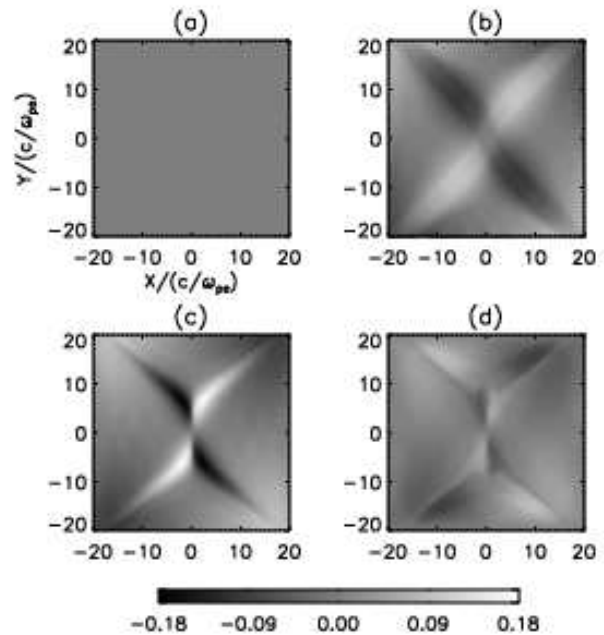


FIG. 5: Time evolution of the spatial distribution of the out-of-plane magnetic field,  $B_z$ , at (a)  $t = 0$ , (b) 100, (c) 170 and (d) 250 for  $\alpha = 1.20$ . The magnetic field intensity is normalised by the initial value,  $B_0$ .

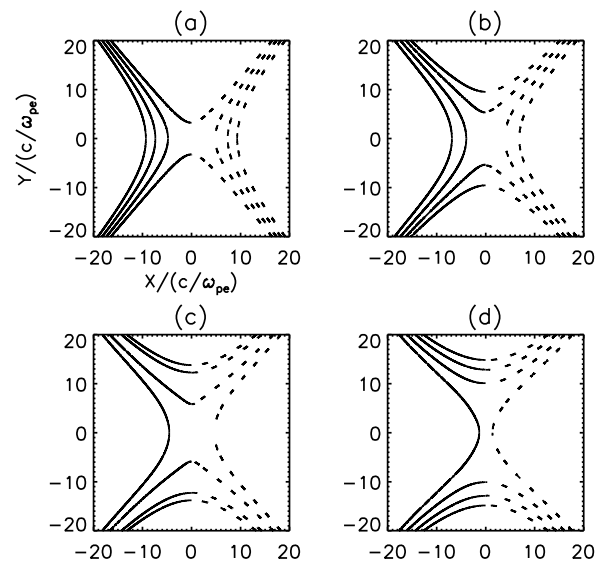


FIG. 6: Time evolution of the magnetic field lines in the  $x$ - $y$  plane at (a)  $t = 0$ , (b) 100, (c) 170 and (d) 250 for  $\alpha = 1.20$ . The several lines are plotted with different intensity,  $|B|/B_0 = 1.55, 1.60, 1.65$  and  $1.70$  on the boundaries. The left and right field lines in the simulation box are distinguished with solid and dotted line styles, respectively, to visualise magnetic field reconnection clearly.

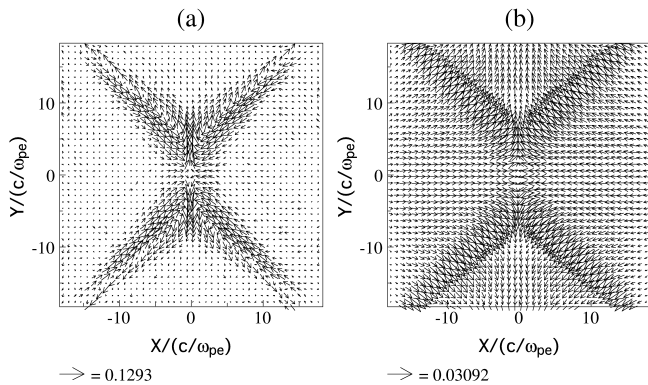


FIG. 7: Electron (a) and ion (b) flow pattern around X-point at  $t = 170$  for  $\alpha = 1.20$ . Note that here  $V_{A0}/c = 0.124$ .

each other in  $x$ -direction, reconnect, and move apart in  $y$ -direction.

Fig. 7 shows electron (a) and ion (b) flows at the peak time of the reconnection. It is rather instructive to see that this figure in effect corroborates the sketch from Ref.[3], [see their Fig. (3.1)]. In particular it shows that the electron and ion flow are clearly separated on the two different spatial scales – electron skin-depth and ion skin-depth, note that since here the mass ratio is 100,  $c/\omega_{pi} = 10c/\omega_{pe}$ . The noticeable difference is caused because they considered initial background magnetic field of Harris-type (anti-parallel), while we study X-point. Naturally, in our case electron inflow into the current sheet is mostly concentrated along the separatrices until they deflect from the current sheet on the scale of electron skin depth, with the electron outflow speeds being of the order of the external Alfvén speed  $0.13c$ . Ion inflow starts to deflect from the current sheet on the ion skin depth scale with the outflow speeds about four times smaller ( $0.03c$ ) than that of electrons. As argued by Ref.[29] it is difference in these two flows which generates the observed quadruple out-of-plane magnetic field.

Fig. 8 shows the local electron energy distribution function near the current sheet at  $t = 0$  (dashed curve) and  $t = 250$  (solid curve) for  $\alpha = 1.20$ . We performed numerical fit to the high energy part of the distribution function ( $E > 0.08m_{e0}c^2 = 41$  keV) and found that the electron distribution has a power law form i.e. in particular the best fit is provided by  $f = dN/dE \propto E^{-4.1}$  (straight solid line). In general, the direct observational evidence for the relation between reconnection and particle acceleration is hard to obtain because acceleration length scale is of the order of ion skin-depth. However, recently it became possible to directly measure electron energy spectrum in the vicinity of X-type region in the Earth’s magneto-tail [30]. They found that from about 2 keV to about 200 keV power law index was between -4.8 and -5.3 (changing in the course of time of the observation). It is interesting to note that both our power law index (-4.1) and the energy ( $0.2 \times m_{e0}c^2 \simeq 0.2 \times 511 \simeq 100$  keV) at the high end of the spectrum are close to the observed

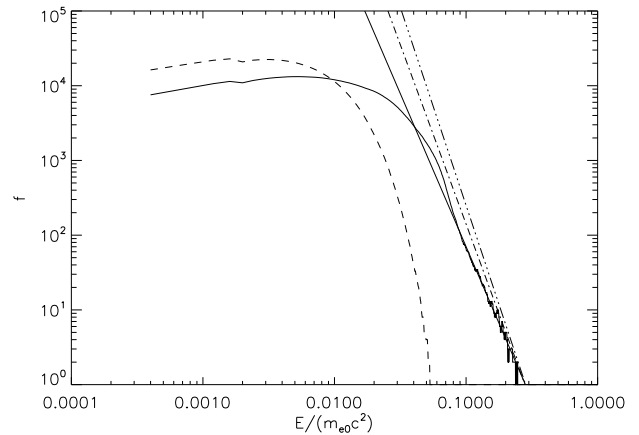


FIG. 8: The local electron energy spectrum (distribution function) near the current sheet at  $t = 0$  (dashed curve) and  $t = 250$  (solid curve) for  $\alpha = 1.20$ . Data is produced using region near the maximum current sheet generation ( $-2 \leq x \leq 2, -8 \leq y \leq 8$ ). The vertical axis shows the number of electrons with a particular energy. The latter is shown on the horizontal axis (normalised by electron rest energy,  $m_{e0}c^2$ ). Straight solid line is our best fit, while dash-dotted and dash-triple-dotted lines are taken from the observations (see text).

values by Ref.[30]. Note that since the parameters of our simulation are for the solar corona ( $\omega_{ce}/\omega_{pe} = 1.0$ ), and are not even totally realistic for that (e.g. to simplify numerical simulation our  $m_i/m_e$ ,  $v_{te}/c$ , and  $V_{A0}/c$  ratios are not entirely realistic), the absolute values of our simulation quoted in keV should be taken with caution (when comparing them to Earth’s magneto-tail results). Yet we are confident in the correctness of the obtained power law indexes. Also, noteworthy fact is that the whistler wave turbulence, based on Fokker-Planck equation for the electron distribution function, subject to a zero-flux boundary condition (same as ours by a chance), is producing [31] similar power law energy spectrum. Recall that it is standing whistler waves are thought to be mediating reconnection in the Hall regime.

## B. Strongly stressed case ( $\alpha = 2.24$ )

In this subsection we present results of numerical simulation for the case of  $\alpha = 2.24$ , which is regarded as a case of strongly stressed X-point.

Fig. 9 shows the numerical simulation results as in Fig. 3 but for  $\alpha = 2.24$ . To avoid repetition we omitted  $\alpha = 1$  case [dotted line in Fig. 3]. We gather from panel (a) that now reconnection rate attains value of 2.5 at  $t = 45$  ( $0.225\tau_A$ ). In the strongly stressed case, in differ the weakly stressed one,  $E_z$  rebounds and an oscillation is established. We calculated average reconnection rate based on Fig. 9(a) using definition from Eq.(7). The result is  $E_{av} = 0.5$ , a value  $\simeq 10$  times bigger than in the

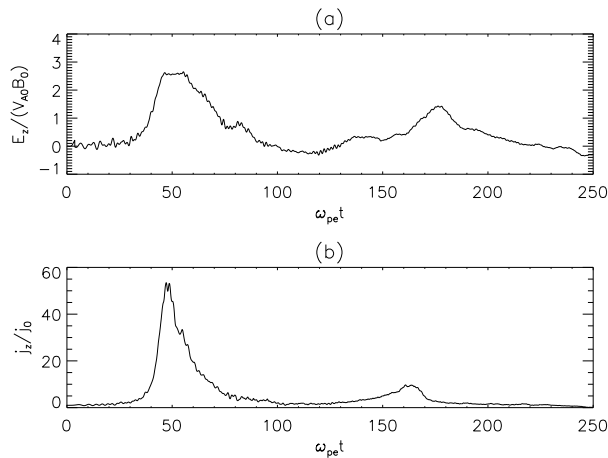


FIG. 9: The same as in Fig. 3 but for  $\alpha = 2.24$ .

weakly stressed case, indicative of more efficient reconnection. Also, much stronger current density,  $j_z/j_0 = 55$ , is generated compared to the weak case [panel (b)] and peak of the reconnection occurs  $170/45 = 3.8$  times earlier. Similar oscillations of current and electric field were used as a mechanism for interpreting the peculiar hard x-ray ( $> 25$  keV) solar flare, which is believed to be produced by a non-thermal electron beam [32, 33].

Fig. 10 panels (a) and (b) show spatial distribution of the  $j_z$  current at the peak of the reconnection  $t = 45$ , and after the current sheet decayed,  $t = 70$ , [the first bounce – see Fig. 9]. The noticeable difference from panels (c) and (d) in Fig. 4 is that now current sheet becomes longer and thinner [the same conclusion reached in Ref.[21], in that large perturbations (strong compression) yields current sheet thinning and onset of more efficient reconnection]. As in the weakly stressed case, we also did the following calculation: Using data from Fig. 10(a) (peak current time snapshot) the width and length of current sheet was estimated by looking at half-width of the  $j_z(x, 0)$  and  $j_z(0, y)$  peak (in both  $x$  and  $y$ -directions). The result is width,  $\delta \simeq 0.4$ , and length,  $\Delta \simeq 17$ . The ratio of the two gives the inflow Mach number  $M_A \simeq \delta/\Delta \simeq 0.02$ . This is 125 times smaller than peak reconnection rate of 2.5 from Fig. 9(a) and 25 times smaller than average reconnection rate of 0.5 from the same figure. This discrepancy can only be attributed to the fact that formula  $M \simeq \delta/\Delta$  only applies to the steady reconnection process. In the case of  $\alpha = 1.2$  the reconnection process was relatively steady thus the latter formula proved a good match, but for  $\alpha = 2.24$  the process is too dynamic and thus  $M_A \simeq \delta/\Delta$  as a measure of reconnection fails. Fig. 10 panels (c) and (d) again show familiar quadruple out-of-plane magnetic field structure, but now it is much more elongated. The panels (e) and (f) where we trace individual magnetic field lines at two different times provide another proof that the reconnection takes place and that the current sheet is now much longer and thinner.

In Fig. 11 is an analog of Fig. 7 but for  $\alpha = 2.24$ .

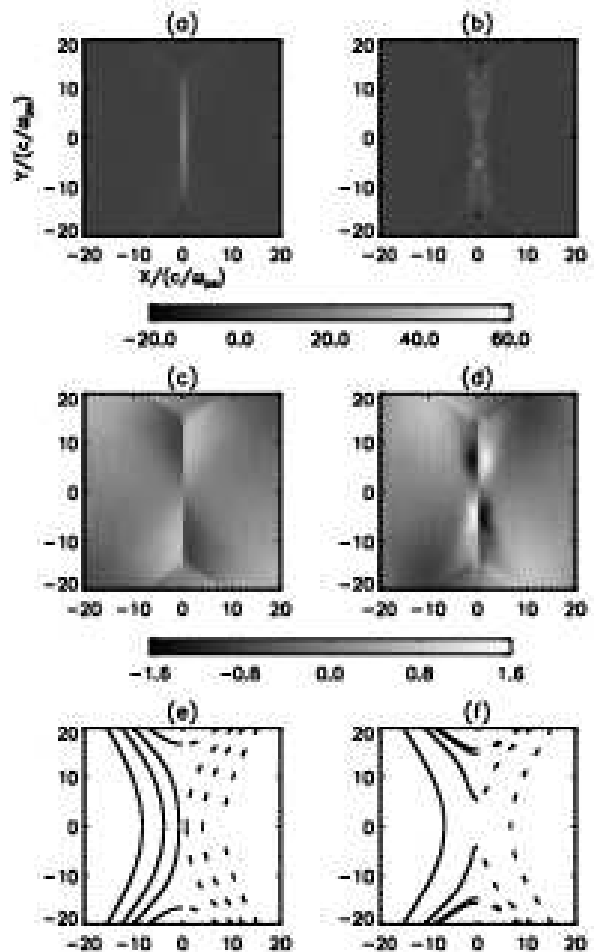


FIG. 10: Spatial distribution of total current density,  $j_z$ , at (a)  $t = 45$  and (b)  $t = 70$  for  $\alpha = 2.24$ . The total current density is normalised by the initial value,  $j_0 = n_0 e v_{A0}$ . The same for out-of-plane magnetic field,  $B_z$ , which is normalised to  $B_0$  at (c)  $t = 45$  and (d)  $t = 70$ . Panels (e) and (f) show individual magnetic field lines with different intensity,  $|B|/B_0 = 2.0, 3.5, 4.0$  and  $4.5$  on the boundaries at  $t = 45$  and (d)  $t = 70$  (f) respectively. The left and right field lines in the simulation box are distinguished with solid and dotted line styles, respectively.

Noteworthy difference from the weak case is that the plasma inflow into the current sheet is perpendicular to it, with the electron outflow speeds reaching external Alfvén Mach number of  $0.5/0.36 = 1.4$  [note arrow length in Fig. 11(a)], and ions again being about four times slower than electrons. Mind that now  $V_{A0}/c = 0.36$ .

Fig. 12 shows the local electron energy distribution function in the current sheet at  $t = 0$  (dashed curve) and  $t = 250$  (solid curve) for  $\alpha = 2.24$ . Note that the dashed curves (corresponding to  $t = 0$ ) in Fig. 8 and Fig. 12 are different. This is due to the fact that different  $\alpha$ 's, mean different initial  $j_0$  current [see Eq.(2)], which contribute to the calculation of the distribution function. We performed numerical fit to the high energy part of the

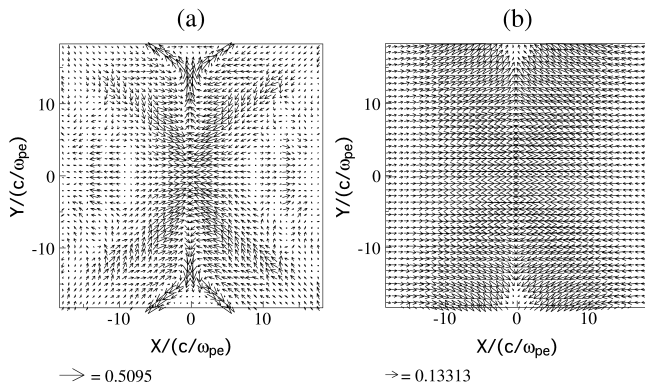


FIG. 11: The same as in Fig. 7 but for  $\alpha = 2.24$ . Here  $t = 45$ . Note that here  $V_{A0}/c = 0.36$ .

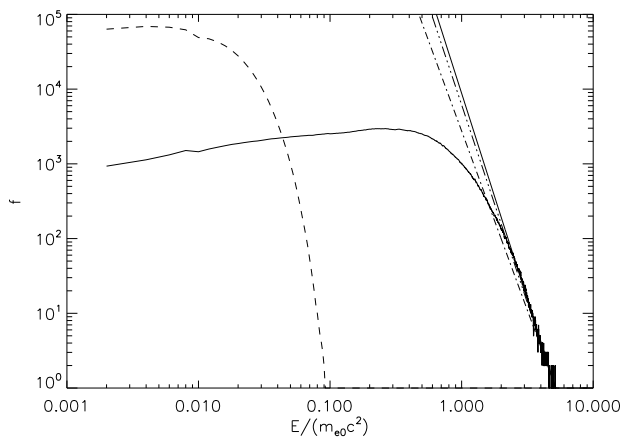


FIG. 12: The same as in Fig. 8 but for  $\alpha = 2.24$ . Here  $t = 250$ . Data is produced using a region near the maximum current generation ( $-1 \leq x \leq 1$ ,  $-16 \leq y \leq 16$ ).

distribution function ( $E > 2.4m_e c^2 = 1.226$  MeV) and found that the electron distribution has the power law index of  $-5.5$  which is quite close to the observed power law range of  $-4.8$  and  $-5.3$  [30]. Note that now attained energies are much higher  $4 \times m_e c^2 \simeq 0.2 \times 511$  keV  $\simeq 2$  MeV (at the high end of the spectrum). Again, we note that values quoted in keV and MeV should be taken with caution [see discussion of Fig. 8 above].

### C. Energetics of the reconnection process

We now try to estimate the efficiency of the X-point collapse by looking at the energetics of the process. In particular in Fig. 13 we plot the magnetic energy,  $E_B(t) = \int \int (B_x^2 + B_y^2 + B_z^2)/(2\mu_0) dx dy$ , for two cases  $\alpha = 1.2$  (solid line) and  $\alpha = 2.24$  (dashed line). The normalisation in each case is  $E_B(0)$ . Note that the latter is different in the both cases because different stress means different initial magnetic field. We gather from this graph

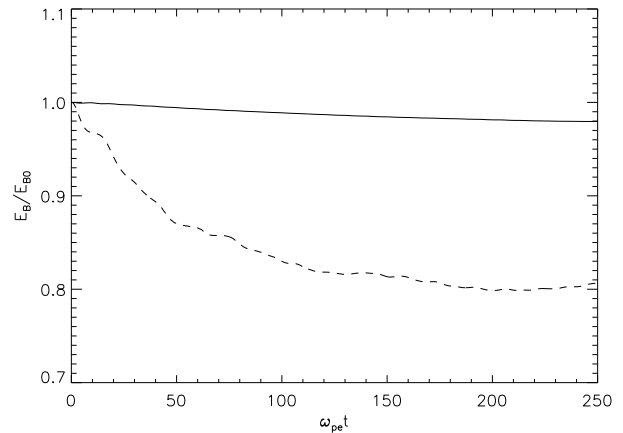


FIG. 13: The magnetic energy,  $E_B(t) = \int \int (B_x^2 + B_y^2 + B_z^2)/(2\mu_0) dx dy$ , normalised on its initial value,  $E_B(0)$ , for two cases  $\alpha = 1.2$  (solid line) and  $\alpha = 2.24$  (dashed line) versus time. Note that  $\omega_{pe} t = 250$  corresponds to 1.25 Alfvén times).

that in the case of weak stress, 2% of the initial magnetic energy (which is a dominant part of the total energy because our plasma beta is 0.02) is converted into heat and energy of super-thermal (accelerated) particles. In the case of large perturbations (strong compression) 20% in the initial magnetic energy is converted into heating and particle acceleration.

## IV. CONCLUSION AND DISCUSSIONS

We studied magnetic reconnection during collisionless, stressed, X-point collapse using kinetic, 2.5D, fully electromagnetic, relativistic Particle-in-Cell numerical code. We investigated two cases of weakly and strongly stressed X-point. Here by weakly and strongly we mean 20% and 124% unidirectional spatial compression of the X-point, respectively. The reconnection rate, defined as the out-of-plane electric field in the magnetic null normalised by the product of external magnetic field and Alfvén speeds, peaks at 0.11 (at 0.85 Alfvén times), with its average over 1.25 Alfvén times being 0.04. We found that during the peak of the reconnection, electron inflow into the current sheet is mostly concentrated along the separatrices until they deflect from the current sheet on the scale of electron skin depth, with the electron outflow speeds being of the order of the external Alfvén speed. Ion inflow starts to deflect from the current sheet on the ion skin depth scale with the outflow speeds about four times smaller than that of electrons. Electron energy distribution in the current sheet, at the high energy end of the spectrum, shows a power law distribution with the index which varies in time, attaining a maximal value of  $-4.1$  at the final simulation time step (this corresponds to 1.25 Alfvén times).

The obtained results in the strongly stressed case show that the magnetic reconnection peak occurs about 3.4 times faster (at 0.25 Alfvén times) and is more efficient. The peak reconnection rate now attains value 2.5 (at 0.25 Alfvén times), with the average reconnection rate over 1.25 Alfvén times being 0.5. Plasma inflow into the current sheet is perpendicular to it, with the electron outflow seeds reaching 1.4 Alfvén external Mach number and ions again being about four times slower than electrons. The power law energy spectrum for the electrons in the current sheet attains now a steeper index of -5.5. This is close to the typical observed power law indexes in the vicinity of X-type region in the Earth's magneto-tail [30].

The reconnection rate versus time figures in both cases indicate that the reconnection has bursty, time-transient behaviour. In the considered two cases, 2% (in weakly stressed) and 20% (in strongly stressed) of the initial magnetic energy is converted into heat and energy of accelerated particles, respectively, both within about one Alfvén time. This is somewhat similar to the previous resistive MHD analog [21] of the present study, in that small perturbation (weak stress) initiates X-point collapse, but then reconnection process is choked off by the gas pressure. At present, it is unclear, however, whether we seem to observe similar behaviour in our simulation. After all, e.g. Petschek mechanism reconnection can be choked off by a different (other than pressure) mechanism [when the diffusion-region inflow magnetic field gets too small [1]].

We also found that in the both cases, during the peak of the reconnection, the quadruple out-of-plane magnetic field is generated. This most is likely to suggest that Hall regime of the reconnection takes place [28].

In addition to the fundamental interest of converting magnetic energy into heat and the energy of accelerated particles, these results are significant for e.g. solar coro-

nal heating problem. It has been estimated that even if only 2% of the magnetic energy in the solar corona is converted into heat, the coronal heating problem would be solved. Also, it is known that the typical resistive diffusion time in the corona is  $10^{15}$  Alfvén times ( $10^8$  years), while the time-transient phenomena such as flares (one of the possible candidates of coronal heating) occur on time scales of 10 – 100 Alfvén times. Our results for the strongly stressed case suggest that 20 % of initial magnetic energy can be released in just 1 Alfvén time. On one hand, one has to realise, that the obtained results are for an X-point configuration, and naturally, the bulk of solar corona is not made of solely of X-points. On the other hand, it is also known that heating of the active regions would provide circa 82 % of the coronal heating budget [34]. In turn, given the fact that X-points are common occurrence in the active regions, our results seem to be of importance for solving the coronal heating problem.

It important to stress that the obtained main result of the 20% conversion of the initial magnetic energy into heat and energy of super-thermal particles, within about one Alfvén time, is obtained in the collisionless regime, thus this result does not suffer from any uncertainty in the anomalous resistivity as in the case of resistive MHD reconnection.

### Acknowledgments

Authors acknowledge use of computational facilities available through UKMHD consortium lead by University of St. Andrews. This research was funded by the United Kingdom's Science and Technology Facilities Council.

- 
- [1] E. Priest and T. Forbes, *Magnetic reconnection: MHD theory and applications* (Cambridge University Press, 2000).
  - [2] D. Biskamp, *Magnetic reconnection in Plasmas* (Cambridge University Press, 2005).
  - [3] J. Birn and E. R. Priest, *Reconnection of magnetic fields: magnetohydrodynamics and collisionless theory and observations* (Cambridge: Cambridge University Press, 2007).
  - [4] J. Birn, J. F. Drake, M. A. Shay, and et al., *J. Geophys. Res.* **106**, 3715 (2001).
  - [5] P. L. Pritchett, *J. Geophys. Res.* **106**, 3783 (2001).
  - [6] J. Birn, K. Galsgaard, M. Hesse, and et al., *Geophys. Res. Lett.* **32**, L06105 (2005).
  - [7] T. D. Arber and M. Haynes, *Physics of Plasmas* **13**, 2105 (2006).
  - [8] K. G. McClements, N. Shah, and A. Thyagaraja, *J. Plasma Phys.* **72**, 571 (2006).
  - [9] G. E. Vekstein and P. K. Browning, *Physics of Plasmas* **4**, 2261 (1997).
  - [10] P. K. Browning and G. E. Vekstein, *J. Geophys. Res.* **106**, 18677 (2001).
  - [11] V. V. Zharkova and M. Gordovskyy, *Astrophys. J.* **604**, 884 (2004).
  - [12] B. Hamilton, L. Fletcher, K. G. McClements, and et al., *Astrophys. J.* **625**, 496 (2005).
  - [13] S. Dalla and P. K. Browning, *Astron. Astrophys.* **436**, 1103 (2005).
  - [14] S. Dalla and P. K. Browning, *Astrophys. J. Lett.* **640**, L99 (2006).
  - [15] P. Browning and S. Dalla, *Mem. Soc. Astron. Italiana* **78**, 255 (2007).
  - [16] Y. E. Litvinenko, *Astron. Astrophys.* **452**, 1069 (2006).
  - [17] J. W. Dungey, *Phil. Mag.* **44**, 725 (1953).
  - [18] V. S. Semenov, M. F. Heyn, and I. V. Kubyshev, *Sov. Astron.* **27**, 660 (1983).
  - [19] G. Vekstein and N. Bian, *Astrophys. J.* **632**, L151 (2005).
  - [20] L. Ofman, P. J. Morrison, and R. S. Steinolfson, *Astrophys. J.* **417**, 748 (1993).

- [21] A. N. McClymont and I. J. D. Craig, *Astrophys. J.* **466**, 487 (1996).
- [22] T. G. Forbes and E. R. Priest, *Astrophys. J.* **446**, 377 (1995).
- [23] J. I. Sakai and Y. Tanaka, *Astron. Astrophys.* **468**, 1075 (2007).
- [24] O. Buneman, *Computer Space Plasma Physics, Simulation Techniques and Software ed. H. Matsumoto & Y. Omura* (Terra Scientific, 1993).
- [25] D. Tsiklauri, J. I. Sakai, and S. Saito, *New J. Phys.* **7**, 79 (2005).
- [26] D. Tsiklauri, J. I. Sakai, and S. Saito, *Astron. Astrophys.* **435**, 1105 (2005).
- [27] J. Heyvaerts and E. R. Priest, *Astron. Astrophys.* **117**, 220 (1983).
- [28] D. A. Uzdensky and R. M. Kulsrud, *Physics of Plasmas* **13**, 2305 (2006).
- [29] M. A. Shay, J. F. Drake, B. N. Rogers, and et al., *J. Geophys. Res.* **106**, 3759 (2001).
- [30] M. Øieroset, R. P. Lin, T. D. Phan, and et al., *Phys. Rev. Lett.* **89**, 195001 (2002).
- [31] C.-Y. Ma and D. Summers, *Geophys. Res. Lett.* **25**, 4099 (1998).
- [32] V. M. Nakariakov, C. Foullon, E. Verwichte, and et al., *Astron. Astrophys.* **452**, 343 (2006).
- [33] L. Ofman and L. Sui, *Astrophys. J.* **644**, L149 (2006).
- [34] M. J. Aschwanden, A. Winebarger, D. Tsiklauri, and et al., *Astrophys. J.* **659**, 1673 (2007).